J. Meas. Sci. Instrum., 2024, 15(4): 547-557. http://jmsi.publish.founderss.cn/
DOI: 10.62756/jmsi.1674-8042.2024054 jmsi@nuc.edu.cn

Optimal design of modular dual-field modulated permanent magnet linear motors with thrust characteristics

MIAO Zhongcui[1,2*], ZHANG Lei[1], LI Yan[1], ZHANG Hui[1]

1. School of Automation & Electrical Engineering, Lanzhou Jiaotong University, Lanzhou 730070, China;
2. Key Laboratory of Opto-Technology and Intelligent Control of Ministry of Education, Lanzhou Jiaotong University, Lanzhou 730070, China

***Corresponding author:** MIAO Zhongcui (miaozhongcui@mail.lzjtu.cn)

Received: April 21, 2023 **Revised:** June 17, 2023 **Accepted:** August 5, 2023

Abstract: To reduce thrust ripple and cost and improve the average thrust of permanent magnet linear motors, a modular dual-field modulation permanent magnet linear motor was studied, and the parameters were optimized. First, sensitive parameters were selected using the Taguchi method, and then the optimal variables were sampled using the optimal Latin hypercube experimental design method and an ensemble of surrogates model of optimization objectives, and its accuracy was verified. Next, a multi-objective particle swarm optimization algorithm was used to optimize the purpose of "maximum average thrust and minimum thrust ripple", and the Pareto front of average thrust and thrust ripple was obtained. Finite element analysis showed that the optimized modular dual flux-modulation permanent magnet linear motor (MDFMPMLM) had a 29.5% reduction in thrust ripple and a 5% increase in average thrust compared to the original motor. This study provided an effective method for improving the performance of permanent magnet linear motors.

Key words: field modulation; thrust characteristics; finite element analysis; ensemble of surrogates model; permanent magnet linear motor; multi-objective optimization

0 Introduction

With the increasing number of super-tall buildings in urban areas, traction elevators face numerous challenges such as long waiting times, high energy consumption, and low floor space utilization[1]. In contrast, the direct-drive ropeless elevator utilizes linear motors to directly drive the cabin, offering advantages such as improved space utilization and operational efficiency. It holds vast potential for applications in the field of high-rise building transportation[2].

The following linear motors are commonly used as drive sources for ropeless elevators, each with its pros and cons. Induction linear motors have a simple structure but lower thrust and more complex control requirements[3]. Permanent magnet synchronous linear motors offer higher thrust but come with higher costs and larger ripple[4]. Magnetic field-modulated permanent magnet linear motors demonstrate advantages in increasing average thrust and suppressing thrust ripple, further progress is still needed to control ripple and reduce costs[5].

To address the issue of thrust ripple, a V-shaped coil was proposed, and the thrust ripple was effectively suppressed by optimizing key structural parameters[6]. Peng et al.[7] used a double V-shaped permanent magnet (PM) structure to reduce end-effect magnetic resistance and minimize thrust ripple. Although these methods have achieved significant results in suppressing thrust ripple, they also negatively impact the motor's average thrust. Song et al.[8] used the equivalent magnetic intensity method to analyze the analytical expressions of air-gap magnetic density and thrust ripple, selected key parameters, and combined with the gravity neighborhood algorithm to achieve the goal of reducing thrust ripple. Miao et al.[9] used sample data to establish a build surrogate model combined with an algorithm for optimization to achieve lower thrust ripple. While analytical modeling has good real-time performance, it can only conduct qualitative analysis. Establishing a surrogate model can improve optimization efficiency. However, its fitting accuracy for optimization objectives using a single surrogate model is low.

Improved average thrust methods mainly involve motor structure design and optimization. Xu et al.[10] utilized a U-shaped magnet structure to increase magnet utilization and

average motor thrust, but pole convexity led to increased thrust ripple. Jia et al.[11] improved average motor thrust by adopting a back-to-back Ω stator with a magnetic focusing rotor. Luo et al. [12] proposed a dual alternate-pole transverse-flux linear motor structure, which reduced pole pitch to increase the operating frequency and thus improved average thrust. Moreover, the fabrication complexity and high manufacturing costs associated with specialized topological structures pose additional obstacles.

Regarding reducing costs, Chunk et al.[13] showed that an alternating pole structure permanent magnet synchronous linear motor, which installed PM according to the table pasting method, had higher PM utilization when the slot number and pole number were the same. Shi et al. [14] proposed a double-sided, PM-type alternating pole vernier linear motor topology structure, which placed a Halbach endless magnet array in the primary core slot to suppress leakage in the space and reduce the amount of PM used. These studies indicated that alternating pole structures could help increase the utilization rate of PM materials, reduce the amount of PM used, and thus reducing manufacturing costs.

To simultaneously reduce thrust ripple, improve average thrust, and reduce the usage of PM materials, a modular dual flux-modulation permanent magnet linear motor (MDFMPMLM) was proposed. Firstly, the evolution of motor topology and its working principle was analyzed. Then, the Taguchi method was employed to perform sensitivity analysis on parameters, and the variables with the most significant impact on the thrust characteristics were selected. Combining an ensemble of surrogates (ES) model and multi-objective particle swarm optimization (MOPSO), the Pareto frontier related to the thrust characteristics was obtained through optimization design. Finally, finite element analysis was utilized to validate the design through simulation.

1 MDFMPMLM structure and operating principle

1.1 MDFMPMLM structure

The conventional modular magnetic field modulated permanent magnet linear motor is shown in Fig. 1(a), where the PM is surface-mounted on the secondary part. The PM is arranged in an alternating pole pattern on the secondary region, as shown in Fig. 1(b). However, this method has weaker excitation intensity and decreased average thrust. The modular flux-reversal permanent magnet linear (MFRPML) motor is designed as a single-phase modular structure, as shown in Fig. 1(c). It can be seen that the modularized alternating pole magnetic field modulated permanent magnet linear motor and the modularized magnetic-flux-reversal permanent magnet linear motor only differ in the installation position of the PM. Therefore, the installation of PM in both the primary and secondary of the engine is considered to obtain the proposed MDFMPMLM structure, as shown in Fig. 1(d).

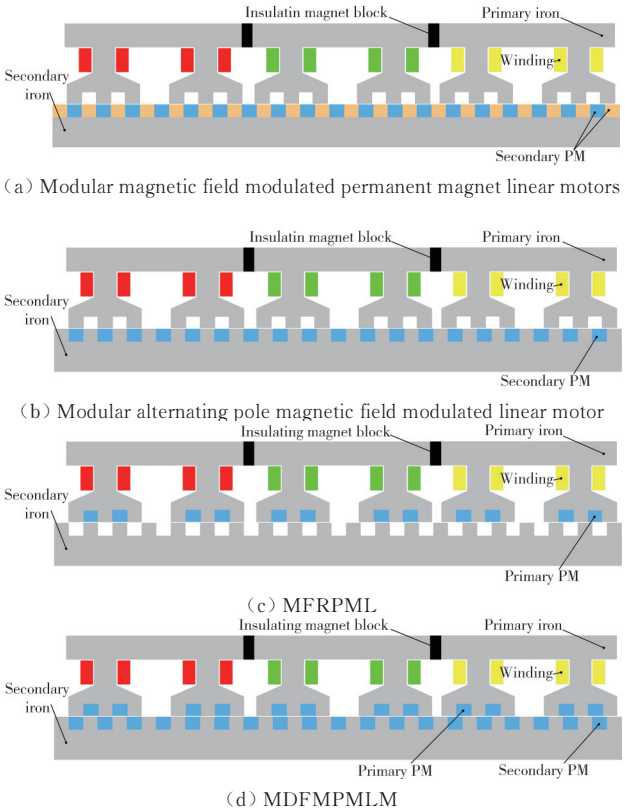

Fig. 1 MDFMPMLM topologies evolution

1.2 Operating principle of MDFMPMLM

According to the theory of magnetic field modulation, MDFMPMLM can be seen as the interaction between the secondary PM/modulation teeth and the primary modulation teeth/PM, resulting in a superposition of magnetic fields. In the case of the modular alternating-pole magnetic field modulation permanent magnet linear motor shown in Fig. 1(b), based on the magnetic potential-gap model analysis, the magnetic potential produced by the secondary excitation unit is

$$F_{es}(x,t)=\sum_{i=1,3,5,\cdots}^{\infty} F_{si}\sin\left[i\frac{2\pi}{L}P_{es}(x-vt)\right], \quad (1)$$

where $F_{es}(x,t)$ is the excitation potential function of the second PM; F_{si} is the amplitude of each harmonic of the excitation potential after Fourier series decomposition of the second PM; P_{es} is the number of pole pairs of the second PM in the effective length of the motor motion direction; v is the movement speed of the secondary

relative to the primary; L is the effective length of the motor motion direction.

At this point, the split teeth of the motor primarily act as modulating teeth, and the air gap permeability function is obtained as

$$\Lambda_m(x)=\Lambda_{m0}+\Lambda_{m1}\cos\frac{2\pi}{L}P_{fm}x, \tag{2}$$

where $\Lambda_m(x)$ is the permeability function of the primary splitting tooth as a modulation unit; Λ_{m0} is the amplitude of the constant term of the permeability function after Fourier level decomposition of the primary splitting tooth; Λ_{m1} is the amplitude of the fundamental term of the permeability function after Fourier level decomposition of the primary splitting tooth; P_{fm} is the number of poles of the primary splitting tooth as a modulation unit.

Therefore, the expression for the air gap flux density of the modular alternating-pole magnetically modulated permanent magnet linear motor during operation can be obtained by

$$B_b(x,t)=F_{es}(x,t)\Lambda_m(x)=\sum_{i=1,3,5,\cdots}^{\infty}\Lambda_{m0}F_{si}\sin\left[i\frac{2\pi}{L}P_{es}(x-vt)\right]+\sum_{i=1,3,5,\cdots}^{\infty}\frac{1}{2}\Lambda_{m1}F_{si}\sin\frac{2\pi}{L}\left[(iP_{es}\pm P_{fm})x-iP_{es}vt\right]. \tag{3}$$

As shown in Fig.1(c), the magnetic potential generated by MFRPMLM during the operation of a primary excitation unit is

$$F_{em}(x)=-\sum_{j=1,3,5,\cdots}^{\infty}F_{mj}\cos\left[j\frac{2\pi}{L}P_{em}x\right], \tag{4}$$

where $F_{em}(x)$ is the excitation potential function of the primary PM; F_m is the amplitude of each harmonic of the excitation potential after Fourier level decomposition of the primary PM; P_{em} is the number of primary PM pole pairs within the effective length of the motor motion direction.

At this point, the alternating pole core of the secondary side serves as the modulating teeth, and the air gap permeability function can be obtained as

$$\Lambda_s(x,t)=\Lambda_{s0}-\Lambda_{s1}\sin\left[\frac{2\pi}{L}P_{fs}(x-vt)\right], \tag{5}$$

where $\Lambda_s(x,t)$ is the permeability function of the secondary splitting tooth as a modulation unit; Λ_{s0} is the amplitude of the constant term of the permeability function after the Fourier level decomposition of the secondary splitting tooth; Λ_{s1} is the amplitude of the fundamental term of the permeability function after Fourier level decomposition of the secondary split tooth; P_{fs} is the number of poles of the secondary splitting tooth as a modulation unit.

Therefore, the air gap flux density expression of the MFRPMLM during operation can be derived as

$$B_c(x,t)=F_m(x)\Lambda_s(x,t)=-\sum_{j=1,3,5,\cdots}^{\infty}\Lambda_{s0}F_{mj}\cos\left[j\frac{2\pi}{L}P_{em}x\right]+\sum_{j=1,3,5,\cdots}^{\infty}\frac{1}{2}\Lambda_{s1}F_{mj}\sin\frac{2\pi}{L}\left[(jP_{em}\pm P_{fs})x\pm P_{fs}vt\right]. \tag{6}$$

Combining Eqs. (3) and (6) to superimpose the air gap flux densities generated by the two sets of PM modulations and jointly contribute to the back electromotive force fundamental wave, it is necessary to satisfy that the number of magnetic pole pairs is the same as the speed of motion. Therefore, there is a clear need to meet

$$\begin{cases}-iP_{em}=\pm P_{fs},\\ |jP_{em}=\pm P_{fs}|=|iP_{es}=\pm P_{fm}|.\end{cases} \tag{7}$$

To satisfy the above equations, it is necessary to ensure

$$\begin{cases}i=j=1,\\ P_{em}=P_{fm}=P_m,\\ P_{es}=P_{fs}=P_s.\end{cases} \tag{8}$$

By utilizing the primary and secondary structures that generate excitation and modulation effects meanwhile through alternate poles, the pole number of the PM as the excitation unit is equal to the number of teeth of the modulation unit, which can satisfy the requirement in Eq. (8). Combining Eqs. (3), (6), and (8), the expression for the air-gap magnetic flux density when the two sets of PM act simultaneously is

$$B_d(x,t)=\frac{1}{2}(F_{m1}\Lambda_{s1}+F_{s1}\Lambda_{m1})\sin\frac{2\pi}{L}\left[(P_s-P_m)x-P_svt\right]. \tag{9}$$

Eq. (9) shows that the superposition of excitation effects from the two sets of PM can be effectively addressed by using the dual-field modulation method, which solves the problem of reduced average thrust due to the adoption of alternate pole distribution in the PM, resulting in a decrease in excitation intensity.

Fig.2(a) shows the three motors air gap flux density waveforms under no-load conditions. The MDFMPMLM has a significantly higher air gap flux density amplitude than the other two motors and almost contains all the higher-order harmonics of the other two motors. In Fig.2(b), the 19th harmonic works with three split teeth on the primary core to produce one pole of the working magnetic field, while the 18th harmonic works with 19 teeth on the secondary body to make one pole of the operating magnetic field.

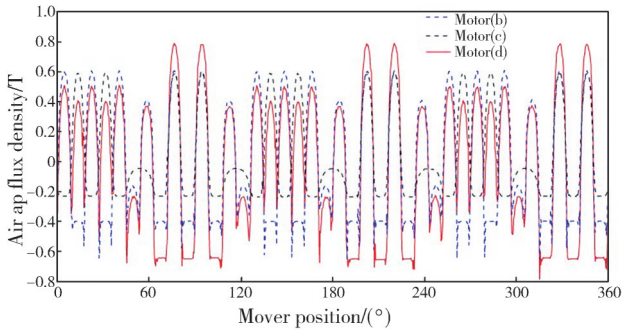

(a) Air gap flux density waveform

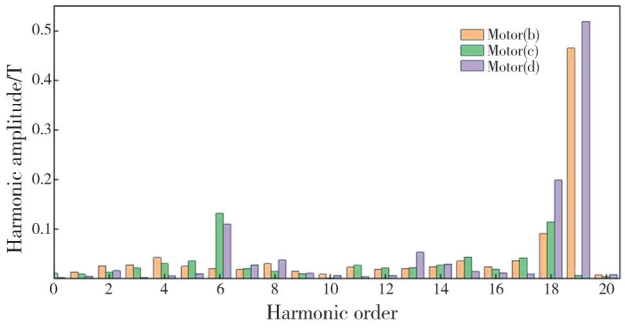

(b) Air-gap flux density distribution of harmonic components

Fig. 2 MDFMPMLM no-load air-gap magnetic density

1.3 Parameters of MDFMPMLM

As the MDFMPMLM adopts a modular design, each phase can be analyzed independently. Fig. 3 shows the topology structure and relevant dimensional variables of the MDFMPMLM. There are a total of 18 parameters, including the primary yoke thickness h_{m3}, slot heights h_{m4} and h_{m2}, slot widths w_{m1} and w_{m2}, inter-tooth width w_{m3}, primary magnet height h_{m1}, magnetization angle θ_m, and arc radius R_m and widths w_{m4}, w_{m5}, and w_{m6}, as well as the secondary magnet height h_s, magnetization angle θ_s, arc radius R_s, and widths w_{s1}, w_{s2} and w_{s3}.

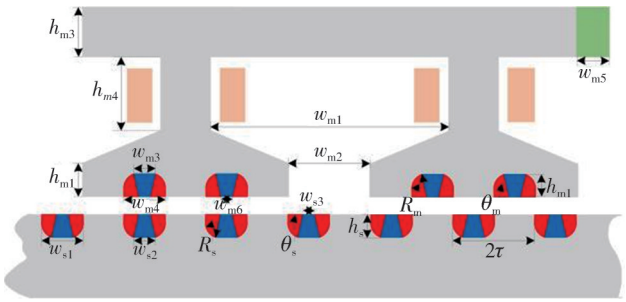

Fig. 3 Topology and related parameters of MDFMPMLM

The initial design values for the 18 parameters are as follows. Primary yoke thickness h_{m3} is 14 mm, slot heights h_{m4} is 18 mm, and h_{m2} is 10 mm, slot widths w_{m1} is 14 mm, and w_{m2} is 26 mm, inter-tooth width w_{m3} is 10 mm, primary magnet heights h_{m1} is 5 mm, magnetization angle θ_m is 0°, arc radius R_m is 1 mm, and widths w_{m4} is 7 mm, w_{m5} is 3 mm, and w_{m6} is 2 mm. Secondary magnet heights h_s is 6 mm, magnetization angle θ_s is 0°, arc radius R_s is 1 mm, widths w_{s1} are 7 mm, w_{s2} is 3 mm, and w_{s3} is 2 mm. Table 1 presents the basic structural parameters of the MDFMPMLM.

Table 1 Basic parameters of MDFMPMLM

Parameter	Value	Parameter	Value
Silicon steel sheet type	50w470	Iron yoke material	steel1010
Number of winding turns	80	Initial polar height	50 mm
PM material	NdFeBN35	Rated speed	1.50 m/s
Air gap length	1 mm	Output power	1.99 KW
Stack thickness	100 mm	Current density	6.80 A/mm^2
Pole distance	14 mm		

In this study, only 4 parameters were analyzed by finite element method (i.e., the height and width of the primary magnet h_{m1} and w_{m4}, and the height and width of the secondary magnet h_s and w_{s1}) to investigate their effects on the thrust characteristics of the MDFMPMLM. The remaining parameters were kept at their original values.

1) Height of primary PM h_{m1} and width w_{m4}

Finite element parametric modeling analysis shows that the size of the primary core side PM and the width of the magnet are two independent design variables that can affect the thrust performance of the motor, as shown in Fig.4.

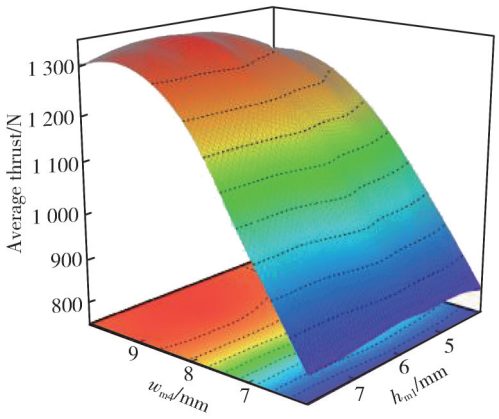

(a) Average thrust

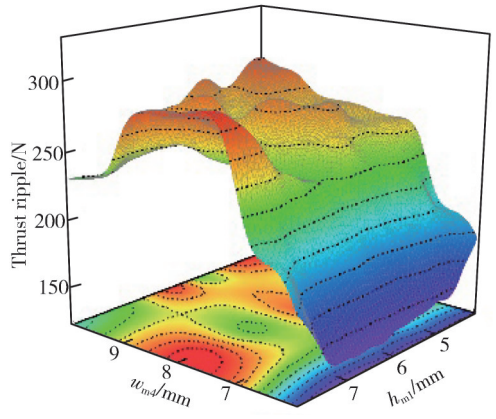

(b) Thrust ripple

Fig. 4 Thrust characteristics as influenced by height and width of PM

The average thrust of the engine delivers a slowly increasing trend with the increase of w_{m4}, while the thrust ripple first decreases and then increases, and h_{m1} also has some influence on the thrust ripple. The comprehensive analysis shows that increasing the PM size can improve the motor's average thrust but will increase thrust ripple and cost. When the size is too large, it will also occupy too much space of the primary core side winding, which will reduce the allowable value of the motor's electric load and is not conducive to reliability assurance. Therefore, the design should be comprehensively considered.

A sector Halbach magnet consisting of two sector PMs and a trapezoidal PM for magnetization were used. Through finite element parameterized analysis, the dimensions of the standard magnetization widths w_{m5} and w_{m6} of the middle trapezoidal PM were optimized to achieve the maximum average thrust and minimum thrust ripple. The optimization results are shown in Fig. 5. Fig. 5(a) shows that the full average thrust is achieved when w_{m5} is 2.7 mm and w_{m6} is 4 mm. Fig.5(b) shows that the minimum thrust ripple is achieved when w_{m5} is 4.8 mm, and w_{m6} is 3.8 mm. However, the two optimal values are located at different points, so careful consideration is needed in the design process.

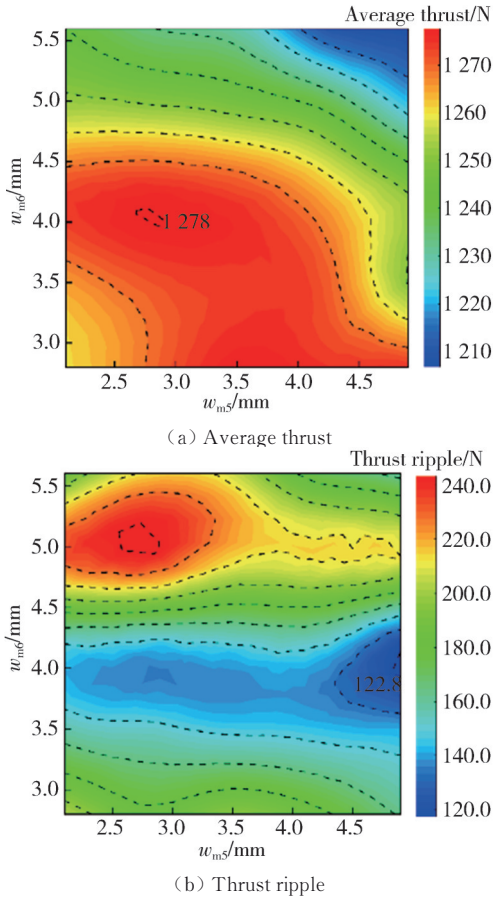

(a) Average thrust

(b) Thrust ripple

Fig. 5 Thrust characteristics as influenced by width of PM

2 Sensitivity analysis of parameters

Due to the large number of parameters affecting the thrust characteristics of MDFMPMLM, to improve the optimization efficiency, the Taguchi method was employed to perform sensitivity analysis on 18 parameters. By using the signal-to-noise (S/N) ratio analysis of Taguchi's method and analysis of variance (ANOVA), sensitive parameters were selected, laying the foundation for subsequent multi-objective optimization. Specifically, the 18 parameters were divided into three groups. The first group included 6 parameters related to the primary magnet, h_{m1}, θ_m, R_m, w_{m4}, w_{m5}, and w_{m6}. The second group included 6 parameters associated with the second magnet, h_s, θ_s, R_s, w_{s1}, w_{s2}, and w_{s3}. And the third group included 6 parameters related to the primary structure, h_{m3}, h_{m4}, h_{m2}, w_{m1}, w_{m2}, and w_{m3}. Sensitivity analysis was then performed on each group of parameters.

2.1 The first set of parameter sensitivity analysis

First, an orthogonal array with 6 variables and 5 levels was established to conduct 25 experiments. Then, the response values for each experiment were calculated using finite element analysis. Finally, S/N ratio analysis and variance analysis were performed on the orthogonal array. The S/N ratio objective for average thrust was set to "larger is better", and the S/N ratio objective for thrust ripple was set to "smaller is better". The analysis results are shown in Table 2 and Fig.6 .

Table 2 ANOVA for the first group of parameters

Parameter	Average thrust		Thrust ripple	
	Variance	Proportion /%	Variance	Proportion /%
h_{m1}	384.80	1.99	95.76	2.30
θ_m	13 151.80	67.94	509.15	12.24
R_m	1 534.60	7.93	1 841.07	44.24
w_{m4}	3 880.65	20.05	1 503.32	36.13
w_{m5}	244.42	1.26	77.93	1.87
w_{m6}	160.76	0.83	133.87	3.22

The analysis showed that θ_m, R_m, and w_{m4} were sensitive parameters for average thrust and thrust ripple. Considering the complexity of the magnetization manufacturing process, θ_m was fixed at 135°. R_m and w_{m4} were determined as optimization variables. The parameters that had a negligible impact on average thrust and thrust ripple were h_{m1}, w_{m5}, and w_{m6}. According to the S/N ratio analysis results, their values were fixed as h_{m1}=6 mm, w_{m5}=2.8 mm, and w_{m6}=4.2 mm.

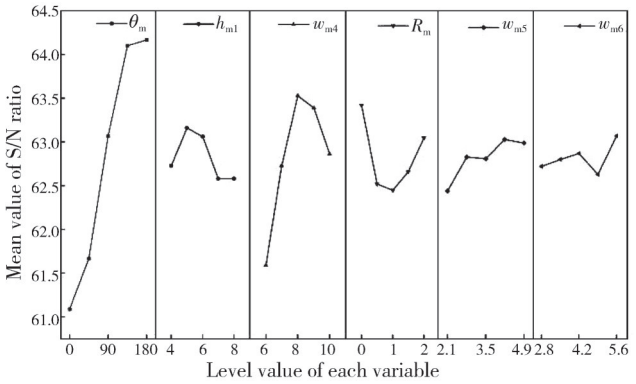

(a) Mean value of S/N ratio for average thrust

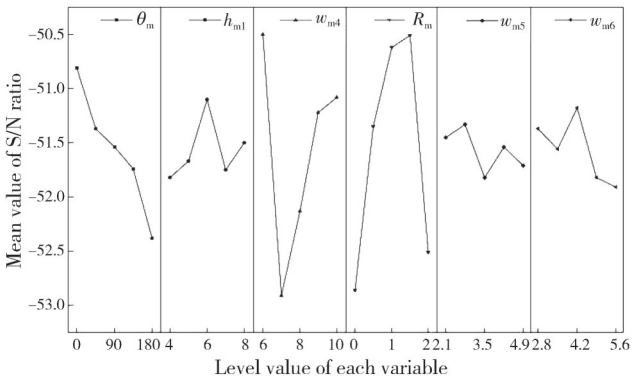

(b) Mean value of S/N ratio for thrust ripple

Fig. 6 S/N analysis of the first group of parameters

2.2 The second set of parameter sensitivity analysis

The same procedure was applied to the second group of parameters. The results are shown in Fig. 7 and Table 3. The analysis results indicate that θ_s, R_s, and w_{s1} are the parameters sensitive to the average thrust and thrust ripple. Considering the complexity of the manufacturing process of magnetization of PM, θ_s is fixed at 45°, R_s and w_{s1} are determined as the optimization variables. Other parameters have a relatively small impact on the average thrust and thrust ripple, and they are fixed at h_s=7 mm, w_{s2}=2.7 mm, and w_{s3}=4.2 mm during optimization.

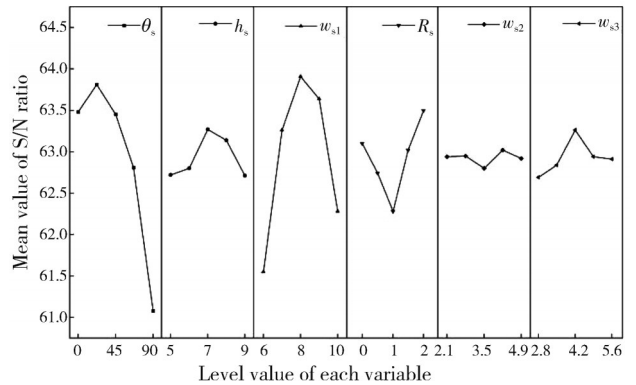

(a) Mean value of S/N ratio for average thrust

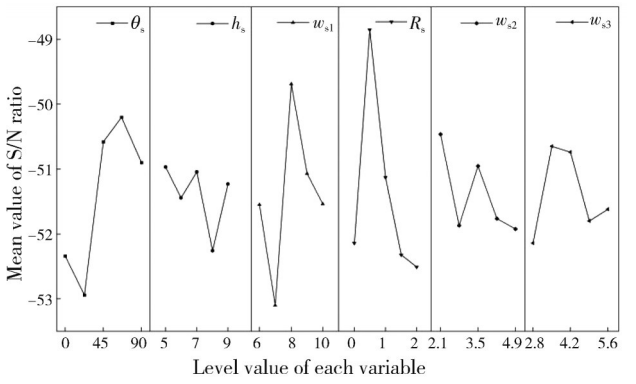

(b) Mean value of S/N ratio for thrust ripple

Fig. 7 S/N ratio analysis of the second group of parameters

Table 3 ANOVA for the second group of parameters

Parameter	Average thrust		Thrust ripple	
	Variance	Proportion /%	Variance	Proportion /%
h_s	446.39	2.60	621.72	6.74
θ_s	7 661.44	44.61	2 153.89	23.35
R_s	1 838.71	10.71	2 919.61	31.64
w_{s1}	6 878.53	40.05	2 067.65	22.41
w_{s2}	312.22	1.82	719.07	8.07
w_{s3}	37.64	0.22	744.31	7.79

2.3 The third group of parameter sensitivity analysis

The same procedure was repeated for the third group of parameters. And the analysis results are shown in Table 4 and Fig.8.

Table 4 ANOVA for the third group of parameters

Parameter	Average thrust		Thrust ripple	
	Variance	Proportion /%	Variance	Proportion/%
h_{m4}	513.50	5.45	119.99	4.92
h_{m3}	105.40	1.12	169.77	6.96
h_{m2}	79.96	0.85	64.52	2.64
w_{m1}	484.99	5.15	103.94	4.26
w_{m2}	8 041.47	85.39	1 891.48	77.49
w_{m3}	191.61	2.03	91.15	3.73

The analysis shows that the parameter sensitive to the thrust characteristics is w_{m2}. Therefore, w_{m2} is determined as the optimization variable. In addition, other parameters have a negligible impact on the thrust characteristics, and they are fixed as h_{m3}=16 mm, h_{m4}=19 mm, h_{m2}=13 mm, w_{m1}=31 mm, and w_{m3}=6 mm.

In summary, the primary slot width w_{m2}, primary PM arc radius R_m, and width w_{m4}, secondary PM arc radius R_s, and width w_{s1} were determined as optimization variables, laying the foundation for multi-objective optimization.

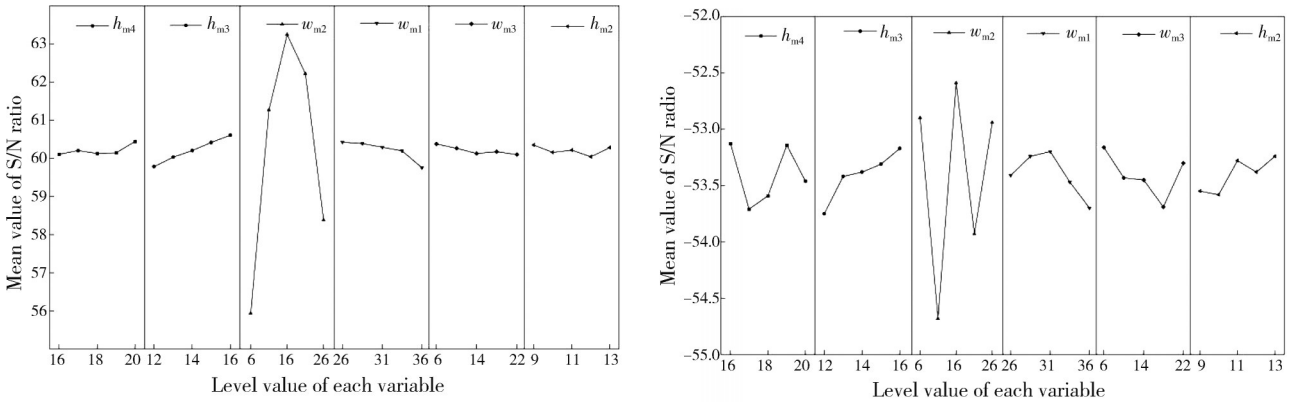

(a) Mean value of S/N ratio for average thrust

(b) Mean value of S/N ratio for thrust ripple

Fig. 8 S/N ratio analysis of the third group of parameters

3 Motor structure optimization

3.1 Optimized solutions

The optimization process in this study consisted of 3 steps. The flowchart of this process is shown in Fig.9. Firstly, a parameterized model was built for the MDFMPMLM structure. Secondly, an optimal Latin hypercube design (OLHD) method was used to sample the motor parameters sensitive to the thrust characteristics, and the simulation response values were calculated. Then, an optimized combination of variables was constructed using a surrogate model. Finally, a multi-objective optimization design was performed on the motor structure based on the surrogate model and the particle swarm algorithm, and the optimal structural parameters were obtained.

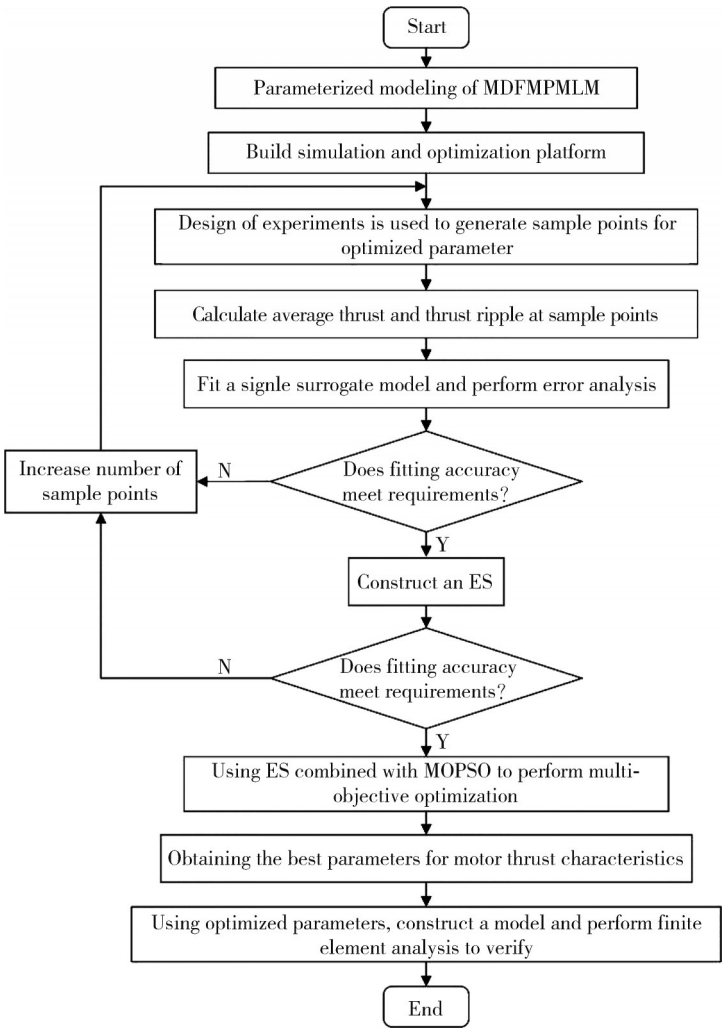

Fig. 9 Multi-objective optimization process

Then the optimized parameters were used to build a finite element model for simulation validation, and the thrust characteristics before and after optimization were compared.

3.2 Optimized parameters

3.2.1 Design variables

Based on the sensitivity analysis of the motor parameters, w_{m2}, R_m, w_{m4}, R_s, and w_{s1} are optimized to improve the thrust performance, which is represented as

$$\boldsymbol{x}=[x_1,x_2,x_3,x_4,x_5]=[w_{m2},R_m,w_{m4},R_s,w_{s1}]. \quad (10)$$

3.2.2 Objective function

The optimization objectives are used to obtain higher average thrust f_1 and lower thrust ripple f_2. The objective function can be expressed as

$$\begin{cases} \min f_1=-\dfrac{F_{rms}(x)}{F_{rms0}(x)}, \\ \min f_2=\dfrac{F_{pk2pk}(x)}{F_{pk2pk0}(x)}, \end{cases} \quad (11)$$

where F_{rms} is the practical value of thrust in one cycle, i.e., the average thrust, and the corresponding F_{rms0} is the original value of the average thrust; F_{pk2pk} is the peak-to-peak value of thrust in one cycle, i.e., the thrust ripple, and F_{pk2pk0} is the initial value of the thrust ripple.

3.2.3 Constraints

For the optimization of the motor structure, the finalized optimized structural variable constraints are shown in Table 5, based on the dimensional relationship of the motor structure and combined with previous design experience.

Table 5 Constraints for optimization parameters

Parameter	w_{m2}/mm	R_m/mm	w_{m4}/mm	R_s/mm	w_{s1}/mm
Initial value	14	1	7	1	7
Lower limit	6	0	6	0	6
Upper limit	26	2	10	2	10

3.3 Experiment

The OLHD method was employed to obtain the samples. Compared with the random Latin hypercube design (RLHD) method, OLHD can improve the uniformity and accuracy of the sample distribution in the design space. As shown in Fig.10, OLHD can result in a more accurate fit between the parameters and the responses. The spatial dimensions of the samples are set to 5, with 70 sample points, and the actual response values of each sample point are calculated using Maxwell.

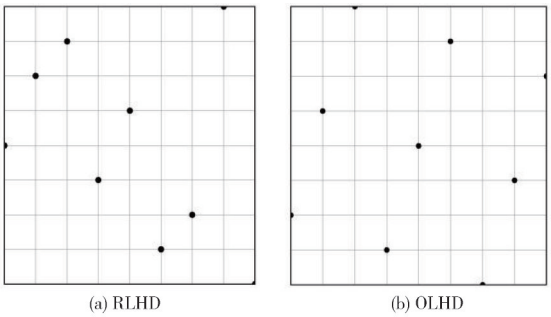

(a) RLHD (b) OLHD

Fig. 10 Distribution of test points for RLHD and OLHD

3.4 Constructing ES

The surrogate model establishes the approximate function relationship between input and output[15]. It has been widely used in engineering optimization design and can effectively reduce the calculation cost of numerical simulation. Compared to a single surrogate model, an ES demonstrates better robustness[16]. Therefore, the SRGTSToolbox in MATLAB was utilized to construct an ES for average thrust and thrust ripple using a weighted linear combination of the response surface method (RSM)[17], Kriging[18], and radial basis function (RBF)[19]. The evaluation criterion for the prediction accuracy is the R^2[20]. The mathematical expression for the ES can be formulated as

$$y_{com}(x)=\sum_{i=1}^{m}\lambda_i(x)\,y_i(x), \quad (12)$$

where $y_{com}(x)$ represents the output response of the ES. Each y_i represents the output response of the ith individual surrogate model. The total number of surrogate models is denoted by m. The weight coefficient λ_i corresponds to the ith surrogate model, and the sum of all weight coefficients λ_i equals 1.

The prediction accuracy of a composite approximation model depends on the weighting coefficients assigned to each approximation model. Higher weighting coefficients are assigned to the individual approximation models with higher prediction accuracy. Considering the computational cost of model accuracy evaluation, a heuristic computational method is adopted to solve the weighting coefficients.

$$\lambda_i=\frac{\lambda_i^*}{\sum_{i=1}^{m}\lambda_i^*}, \quad (13)$$

$$\lambda_i^*=\left(E_i+\alpha\overline{E}\right)^{\beta},\ \alpha<0,\beta<0, \quad (14)$$

$$E_i=GMSE_i, \quad (15)$$

$$\overline{E}=\frac{\sum_{i=1}^{m}E_i}{m}, \tag{16}$$

where E_i represents the generalized mean square error (GMSE) of the ith individual surrogate model, while E denotes the average GMSE of all individual surrogate models; the parameter α indicates the significance level of the average GMSE, while β represents the importance level of the accuracy metrics for each surrogate model. When α is set to 0.05 and β is set to -1, the ES exhibits higher prediction accuracy and better stability.

Based on the experimental design with sample points and corresponding output responses, 3 individual surrogate models, namely RSM, RBF, and Kriging were constructed. Cross-validation was performed using randomly selected sample points to assess the accuracy of these individual surrogate models based on metrics such as the R^2. By solving Eqs. (13) to (16), the optimal weight coefficients for each surrogate model in the ES were determined. The fitting accuracy of each surrogate model and the corresponding weight coefficients are presented in Table 6.

Table 6 Surrogate models R^2 and weight factor

Response	Parameter	RSM	Kriging	RBF	ES
Average thrust	R^2	0.942	0. 905	0.863	0.982
	Weighting factor	0.452	0.364	0.184	—
Thrust ripple	R^2	0.907	0.950	0.901	0.978
	Weighting factor	0.253	0.527	0.22	—

Based on the analysis conducted above, it is evident that the R^2 for both average thrust and thrust ripple in the ES is higher than that of the individual surrogate models. This finding indicated that the proposed ES could be effectively utilized in subsequent optimization designs.

3.5 Multi-objective optimization

ES combined with the MOPSO algorithm was used for the multi-objective optimization of the MDFMPMLM to obtain the globally optimal structural parameters of the motor[21]. The particle swarm algorithm has a simple structure, and its main components are the update formulas for particle velocity and position, namely

$$\begin{cases} v_i = wv_i + c_1 rand()(pbex_i - x_i), \\ +c_2 rand()(gbest_i - x_i), \\ x_i = x_i + v_i, \end{cases} \tag{17}$$

where v_i is the particle velocity; x_i is the particle position; ω is the inertia weight; $rand()$ is a random number between (0, 1); c_1 and c_2 take a fixed value of 2.05.

The MDFMPMLM structure's ES was subjected to multi-objective optimization design using MATLAB, and the convergence of the MOPSO algorithm was determined through multiple iterations. After 600 iterations, the MOPSO algorithm showed slight variation, indicating that the optimization had reached a stopping condition.

The Pareto front distribution obtained after multiple iterations is shown in Fig. 11, and the optimal design solutions A, B, and C are selected for comparison with the initial design, as shown in Table 7.

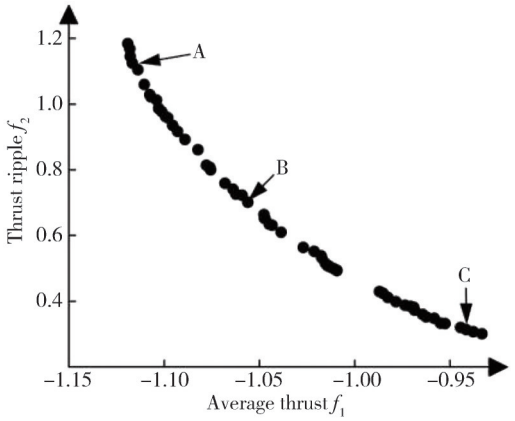

Fig. 11 Pareto front of MOPSO at 600 iterations

Table 7 MDFMPMLM parameters optimization results

Parameter	w_{m2}/mm	R_m/mm	w_{m4}/mm	R_s/mm	w_{s1}/mm
Initial Value	14	1	7	1	7
Point A	16.1	1.8	9	7.8	1.7
Point B	15.1	1.7	9.4	7.4	1.6
Point C	15	1.4	9.5	6.2	1.7

3.6 Finite element simulation verification

A finite element model was developed using the initial and optimized parameters to verify the optimization results and analyze the motor's average thrust and thrust ripple. The analysis results are shown in Table 8 and Fig.12.

Table 8 MDFMPMLM optimization results

Parameter	Average thrust/N	Thrust ripple/N	Volume of PM/cm^3	Utilization of PM/(N•L^{-1})
Initial	1 270	113.5	150	8 200.6
Point A	1 411.4	136.2	170	8 376.4
Point B	1 333.9	80.1	160	8 032.5
Point C	1 227.4	43.2	150	8 200.2

It can be observed that if the main goal is to increase the average thrust, the average thrust of the point A motor is increased by 11.1%, but the thrust ripple is also increased. Although it achieves the highest growth in average thrust per unit volume of the PM, it does not effectively suppress the thrust ripple. If both reducing thrust ripple and

improving average thrust are considered, the motor at point B reduces the thrust ripple by 29.5% compared to the original engine while increasing the average thrust by 5.0%. On the other hand, if the main objective is to reduce the thrust ripple, the motor at point C achieves a minor thrust ripple, reducing it by 61.9%. Still, the corresponding average thrust decreases by 3.0% compared to the original. Considering the elevator operation requirements, a balance must be made between the average thrust and the thrust ripple. Therefore, improving the average thrust while suppressing the thrust ripple is best achieved at point B.

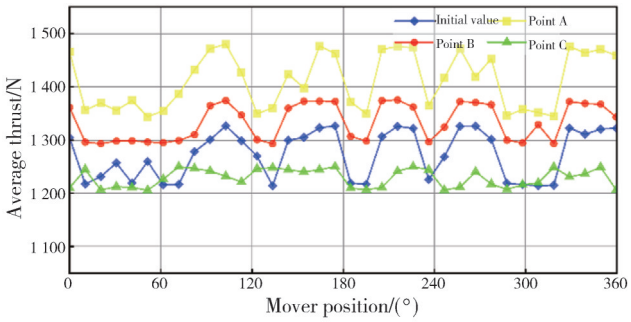

(a) Average thrust

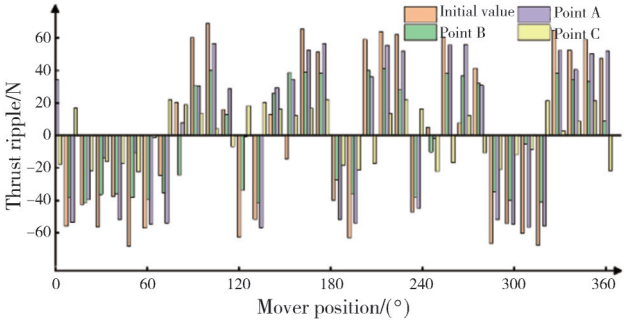

(b) Thrust ripple

Fig. 12 Thrust characteristic analysis for initial and optimized values

4 Conclusions

A novel MDFMPMLM structure was proposed that significantly reduced the amount of used PM material and improved the thrust characteristics compared to traditional surface-mounted PM linear motors. Double-field modulation was employed to superimpose the excitation effects of the primary and secondary PM arrays to address the problem of decreased average thrust caused by the declining excitation intensity of the secondary when using alternate pole excitation. A single-phase modular design was introduced to mitigate thrust ripple caused by three-phase asymmetry. In addition, due to the large number of parameters affecting the thrust characteristics of MDFMPMLM, these variables are optimized in this paper.

In the optimization design, the Taguchi method was used to conduct sensitivity analysis on the parameters, and it was found that the primary slot width w_{m2}, the primary magnet arc radius R_m, and width w_{m4}, the secondary magnet arc radius R_s, and width w_{s1} were the sensitive variables affecting the thrust characteristics. Then, the selected variables were subjected to optimal Latin hypercube experimental design, and MOPSO assisted with ES. Finally, points A, B, and C were set for finite element analysis with initial values. The results showed that the optimized MDFMPMLM reduced thrust ripple by 29.5% and increased average thrust by 5.0%.

The MDFMPMLM structure had the advantages of reduced thrust pulsation, improved thrust characteristics, low manufacturing cost, good electromagnetic compatibility and so on. Therefore, this structure was more conducive to the application of cordless elevator system.

References

[1] LI S. Report on the work of the 8th council meeting of china elevator association. China Elevator, 2023, 34(5): 14-22.

[2] FAN H, CHAU K T, LIU C H, et al. Quantitative comparison of novel dual-PM linear motors for ropeless elevator system. IEEE Transactions on Magnetics, 2018, 54(11): 8106506.

[3] MORIZANE T, MASADA E. Study on the feasibility of application of linear induction motor for vertical movement. IEEE Transactions on Magnetics, 1993, 29(6): 2938-2940.

[4] KOU B, LUO J, YANG X, et al. Modeling and analysis of a novel transverse-flux flux-reversal linear motor for long-stroke application. IEEE Transactions on Industrial Electronics, 2016, 63(10): 6238-6248.

[5] LING Z J, ZHAO W X, JI J H, et al. Overview of high-thrust permanent magnet linear actuator and its key technologies. Transactions of China Electrotechnical Society, 2020, 35(5): 1022-1035.

[6] ZONG K F, ZHAO J W, SONG J C, et al. Thrust ripple suppression of v-shaped coil permanent magnet synchronous linear motor. Proceedings of the Chinese Society of Electrical Engineering, 2019, 39(22): 6736-6746.

[7] PENG B, LI L P, ZHANG N, et al. Method for reducing cogging force ripple of double v-structure permanent magnet linear motor. Transactions of China Electrotechnical Society, 2017, 32(22): 108-114.

[8] SONG J C, DONG F, ZHAO J E, et al. Optimization design of coreless permanent magnet synchronous linear motor based on gravity neighborhood algorithm. Proceedings of the Chinese Society of Electrical Engineering, 2017, 37(12): 3594-3601.

[9] MIAO Z C, SU Y. Analysis of detent force in flat-type permanent magnet linear synchronous motor and multi-objective optimization based on parameter classification. IEEJ Transactions on Electrical and Electronic Engineering, 2022, 17(12): 1772-1782.

[10] XU X Z, FENG H C, AI L W, et al. U-shaped permanent magnet convex-pole linear motor: structure and

electromagnetic characteristics. Transactions of China Electrotechnical Society, 2021, 36(6): 1179-1189.
[11] JIA Z, YANG W P, HE W, et al. Back-to-back Ω stator transverse flux permanent magnet linear motor. Proceedings of the Chinese Society of Electrical Engineering, 2022, 42(21): 7964-7972.
[12] LUO J, KOU B Q, YANG X B. Optimization and design of double alternating pole transverse flux linear motor. Transactions of China Electrotechnical Society, 2020, 35(5): 991-1000.
[13] CHUNG S U, LEE H J, WOO B C, et al. A feasibility study on a new doubly salient permanent magnet linear synchronous machine. IEEE Transactions on Magnetics, 2010, 46(6): 1572-1575.
[14] SHI C J, LI D W, QU R H, et al. A novel linear permanent magnet vernier machine with consequent-pole permanent magnets and Halbach permanent magnet arrays. IEEE Transactions on Magnetics, 2017, 53(11): 2501404.
[15] DONG X J, CHEN Q, LIU W B, et al. A systematic framework of constructing surrogate model for slider track peeling strength prediction. Science China(Technological Sciences), 2024, 67(10): 3261-3274.
[16] VIANA F A C, HAFTKA R T, STEFFEN V. Multiple surrogates: how cross-validation errors can help us to obtain the best predictor. Structural and Multidisciplinary Optimization, 2009, 39(4): 439-457.
[17] KAZEMIAN A, KHOSRAVI K, SEN S, et al. Optimizing photovoltaic thermal systems with wavy collector Tube: a response surface-based design study with desirability analysis. Applied Thermal Engineering, 2025, 258(PA): 124475-124475.
[18] JIN X, GUO P H, LI J Y. Multi-objective multi-variable large-size fan aerodynamic optimization by using multi-model ensemble optimization algorithm. Journal of Thermal Science, 2024, 33(3): 914-930.
[19] HAN H H, WANG J, CHEN S, et al. Product quality prediction based on RBF optimized by firefly algorithm. Journal of Systems Engineering and Electronics, 2024, 35(1): 105-117.
[20] CHEN H, LI W K, CUI W C, et al. A pointwise ensemble of surrogates with adaptive function and heuristic formulation. Structural and Multidisciplinary Optimization, 2022, 65(4): 113.
[21] XU Z X, ZHU S R. Multi-objective particle swarm optimization by fusing multiple strategies. Journal of Measurement Science and Instrumentation, 2022, 13(3): 284-299.

模块化双磁场调制永磁直线电机推力特性的优化设计

缪仲翠[1,2*], 张　磊[1], 李　燕[1], 张　慧[1]

1. 兰州交通大学 自动化与电气工程学院, 甘肃 兰州 730070;
2. 兰州交通大学 光电技术与智能控制教育部重点实验室, 甘肃 兰州 730070

摘　要: 为了降低永磁直线电机的推力波动和成本, 提升平均推力, 本文以模块化双磁场调制永磁直线电机为研究对象对电机的结构变量进行了优化。首先, 采用Taguchi法选出敏感性结构变量。然后, 利用最优拉丁超立方试验设计方法对优化变量进行抽样, 并构建优化目标的组合近似模型, 进行精度检验。接着, 采用多目标粒子群优化算法, 以"平均推力最大, 推力波动最小"为目标进行优化, 获得平均推力和推力波动的Pareto前沿。有限元分析表明, 优化后的MDFMPMLM相比原始电机, 推力波动下降了29.5%, 平均推力提升了5%。这项研究为永磁直线电机的性能改善提供了有效方法。

关键词: 磁场调制; 推力特性; 有限元分析; 组合近似模型; 永磁直线电机; 多目标优化

引用格式: MIAO Zhongcui, ZHANG Lei, LI Yan, et al. Optimal design of modular dual-field modulated permanent magnet linear motors with thrust characteristics. Journal of Measurement Science and Instrumentation, 2024, 15(4): 547-557.